

MaIR: A Locality- and Continuity-Preserving Mamba for Image Restoration

Boyun Li
Sichuan University
Chengdu, China

liboyun.gm@gmail.com

Haiyu Zhao
Sichuan University
Chengdu, China

haiyuzhao.gm@gmail.com

Wenxin Wang
Sichuan University
Chengdu, China

wangwenxin.gm@gmail.com

Peng Hu
Sichuan University
Chengdu, China

penghu.ml@gmail.com

Yuanbiao Gou
Sichuan University
Chengdu, China

gouyuanbiao@gmail.com

Xi Peng
Sichuan University
Chengdu, China

pengx.gm@gmail.com

Abstract

Recent advancements in Mamba have shown promising results in image restoration. These methods typically flatten 2D images into multiple distinct 1D sequences along rows and columns, process each sequence independently using selective scan operation, and recombine them to form the outputs. However, such a paradigm overlooks two vital aspects: i) the local relationships and spatial continuity inherent in natural images, and ii) the discrepancies among sequences unfolded through totally different ways. To overcome the drawbacks, we explore two problems in Mamba-based restoration methods: i) how to design a scanning strategy preserving both locality and continuity while facilitating restoration, and ii) how to aggregate the distinct sequences unfolded in totally different ways. To address these problems, we propose a novel Mamba-based Image Restoration model (MaIR), which consists of Nested S-shaped Scanning strategy (NSS) and Sequence Shuffle Attention block (SSA). Specifically, NSS preserves locality and continuity of the input images through the stripe-based scanning region and the S-shaped scanning path, respectively. SSA aggregates sequences through calculating attention weights within the corresponding channels of different sequences. Thanks to NSS and SSA, MaIR surpasses 40 baselines across 14 challenging datasets, achieving state-of-the-art performance on the tasks of image super-resolution, denoising, deblurring and dehazing. Our codes will be available after acceptance.

1. Introduction

Image restoration aims to recover visually appealing high-quality images from given degraded correspondences, *e.g.*, noisy, blurry, and hazy images. In recent years, the meth-

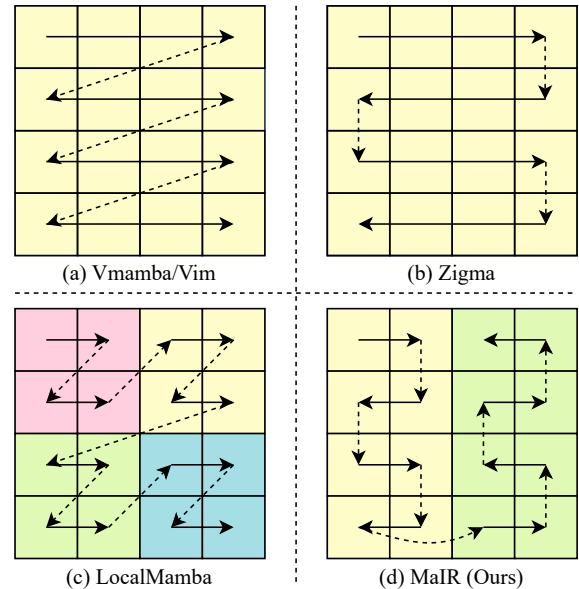


Figure 1. The scanning strategies in existing Mamba-based methods and our proposed method. (a) **Vmamba/Vim** uses Z-shaped scan path to flatten 2D image into 1D sequences, in which both the locality and continuity of 2D image are disrupted. (b) **Zigma** utilizes S-shaped path to maintain spatial continuity, while ignores the locality. (c) **LocalMamba** leverages window-based scanning region to preserve locality. However, the Z-shaped scanning path within and across the windows disrupts the spatial continuity. In contrast, (d) **MaIR** divides images into multiple non-overlapping stripes, and adopts S-shaped scanning path within and across the stripes, thus simultaneously preserves both locality and continuity.

ods based on Convolutional Neural Networks (CNNs) and Transformers have significantly advanced image restoration by effectively capturing locality (*i.e.*, fine-grained patterns and correlations in small regions) and continuity (*i.e.*, smooth, gradual transitions across larger areas) inherent in

2D natural images. To be specific, CNNs capture locality and continuity through the elaborately designed small kernels and sliding strides, respectively. Transformers capture them through local window partitions and adjacent window communications (*e.g.*, window shifts and window expansions). However, like a coin with two sides, the success of CNNs and Transformers in preserving locality and continuity comes at the cost of their ability to capture long-range dependencies. Both of them only consider a limited region of the input image at a time due to their localized kernels or windows, making them challenging to model relationships that span across larger sections of the image. Therefore, it is highly expected to develop a method that is able to capture long-range dependencies while well preserving locality and continuity inherent in 2D natural images.

Mamba [12, 16], a novel selective State Space Model [17], has garnered significant attention due to its promising performance in long sequence modeling while maintaining nearly linear complexity. As Mamba’s core algorithm, Selective Scan Operation (SSO), is inherently designed for 1D sequences, it can not be directly applicable to processing 2D images. To address the problem, Mamba-based restoration methods typically involve a 3-step pipeline: i) flattening 2D image into multiple 1D sequences along rows and columns; ii) processing each sequence independently using SSO; and iii) aggregating the processed sequences to form the output 2D image. However, such a paradigm still faces two demerits when processing images. First, when transforming image into sequences, it disrupts the locality and continuity inherent in image, as illustrated in Fig. 1(a)-(c). Second, it generally aggregates processed sequences via pixel-wise summation, overlooking the distinct contexts among sequences unfolded through totally different ways.

In this work, we present a novel locality- and continuity-preserving Mamba for Image Restoration (MaIR), which consists of Nested S-shaped Scanning strategy (NSS) and Sequence Shuffle Attention block (SSA). Specifically, NSS preserves the locality through stripe-based scanning region, and the continuity via the S-shaped scanning path with shift-stripe mechanism. SSA aggregates the processed sequences by calculating attention weights within corresponding channels of sequences. Thanks to corporation of NSS and SSA, MaIR enjoys the following merits. Firstly, MaIR involves a cost-free solution to preserve the locality and continuity inherent in natural images, ensuring structural coherence and avoiding computational overhead. Secondly, MaIR captures complex dependencies across distinct sequences, facilitating to leverage complementary information from both forward and reversed rows and columns.

To summarize, the contributions and innovations of this work are as below:

- In this work, we present MaIR, an approach that effi-

ciently captures long-range dependencies while preserving the locality and continuity inherent in natural images.

- For Mamba, we introduce NSS, a cost-free solution to preserve locality and continuity, and SSA, a module to capture dependencies across distinct sequences.
- MaIR obtains state-of-the-art performance on four tasks across 14 benchmarks comparing with 40 baselines.

2. Related Works

In this section, we will briefly review related works in image restoration and vision Mamba.

2.1. Image Restoration

According to the focus of this paper, existing methods can be classified into three categories, *i.e.*, CNN-, Transformer- and Mamba-based methods. We will introduce the first two categories here, while the last one is detailed in Sec. 2.2.

CNN-based Method: Benefiting from the ability of capturing locality and continuity in natural images, CNN-based methods have achieved promising results in various tasks of image restoration, such as image super-resolution [11, 27, 29, 40, 64], image denoising [15, 26, 44, 57, 65] and image deblurring [39, 39, 48, 60]. However, since their localized receptive fields, CNNs are inherently limited in capturing long-range dependencies.

Transformer-based Method: Transformers are theoretically capable of capturing the global dependencies [53, 66]. However, to avoid impractical quadratic complexity on images, existing methods [7, 28, 33] tend to partition the local regions of input image into different windows, and calculate attentions within or across the windows. For instance, SwinIR [28] computes attentions within local windows and shifts these windows between layers. HAT [7] divides images into overlapping windows to enhance the interaction between neighbor windows. Although these methods have ensured structural coherence (*i.e.*, locality and continuity) of natural images and avoided computational overhead, they fell into another dilemma of failing to fully capture long-range dependencies due to their limited window sizes.

2.2. Vision Mamba

Due to Mamba’s demonstrated superiority in long-sequence modeling [9, 17, 46], some studies have introduced it into high- [22, 32, 70] and low-level [13, 19, 67] vision tasks. To enable SSO to process images, these methods [32, 70] tend to flatten 2D images into multiple 1D sequences along the different directions. For instance, Vmamba [32] proposes cross-scan strategy which flattens input images along rows and columns. However, existing scanning strategies disrupt structure coherence which is essential for image restoration. Recently, some Mamba-based restoration methods have begun to recognize the importance of structure coherence, and tend to introduce extra coherence-preserving modules. For

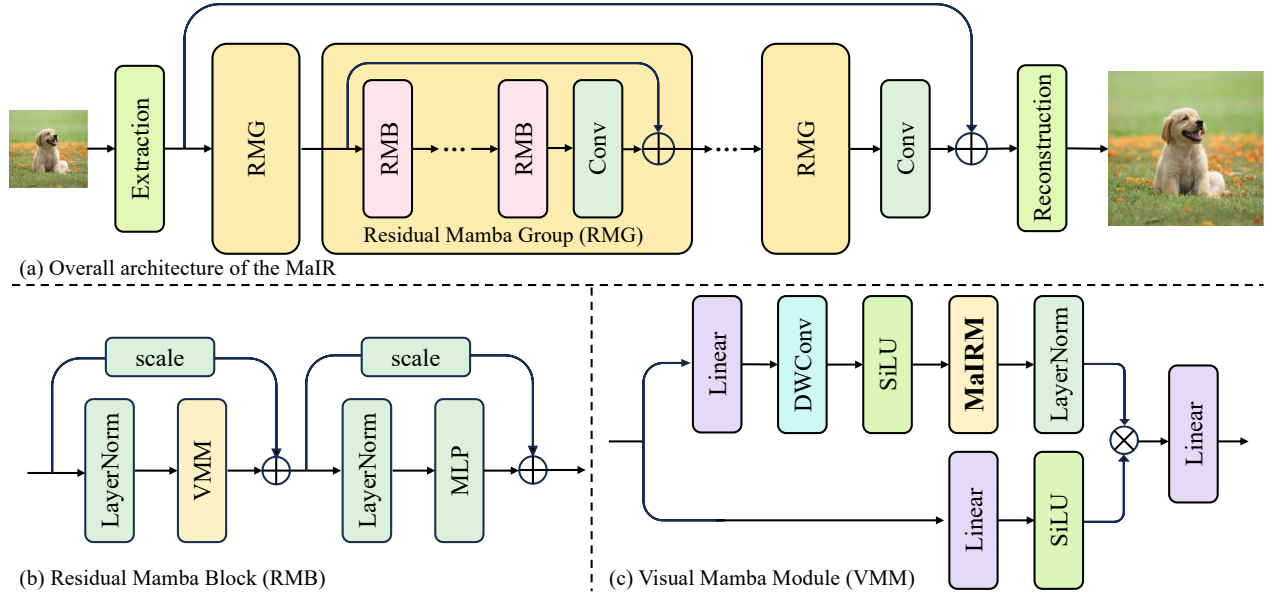


Figure 2. Illustrations of MaIR. (a) The overall architecture of MaIR, highlighting its core component, Residual Mamba Group (RMG). RMG is primarily composed of (b) Residual Mamba Block (RMB), in which (c) Visual Mamba Module (VMM) plays a pivotal role.

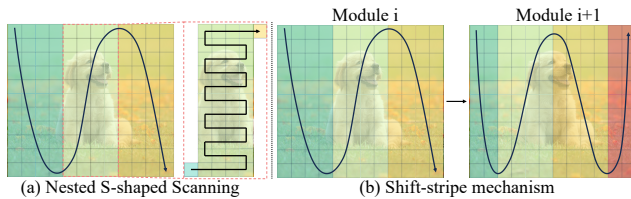


Figure 3. Illustrations of (a) Nested S-shaped Scanning strategy (NSS) and (b) shift-stripe mechanism.

instance, MambaIR [19] and UVM-Net [67] enhances locality through additional CNN layers, but introduces extra computational costs. Although some other studies [20, 22] devote to designing scanning strategy to preserve locality and continuity, most of them can only preserve one of them. In contrast, MaIR provides a cost-free solution to preserve both locality and continuity.

3. Methods

In this section, we first introduce the overall architecture of our MaIR, and then elaborate on NSS and SSA assembled in MaIR Module (MaIRM).

3.1. Overall Architecture

Network Structure: Following previous works [19, 28], MaIR is built up with three stages, namely, shallow feature extraction stage, deep feature extraction stage and reconstruction stage. Specifically, in the shallow feature extraction stage, for a given degraded image $x \in \mathcal{R}^{3 \times H \times W}$, we first employ a convolution layer to extract shallow feature $F_S \in \mathcal{R}^{C \times H \times W}$, where H and W represent the height and

width of x , and C is the number of channels. After that, F_S is fed to the deep feature extraction stage to produce deep feature $F_D \in \mathcal{R}^{C \times H \times W}$. As illustrated in Fig. 2, the deep feature extraction stage is stacked by multiple Residual Mamba Groups (RMGs), where each RMG consists of several Residual Mamba Blocks (RMBs). Within each RMB, a Visual Mamba Module (VMM) is introduced to capture long-range dependencies, which is further composed of our proposed MaIRM. Finally, we reconstruct the high-quality image based on F_S and F_D . Specifically, for image super-resolution, we introduce a pixel-shuffle layer $U_{ps}(\cdot)$ and a 3×3 convolution layer $\Phi_{3 \times 3}(\cdot)$ to reconstruct the high-resolution image $y' = \Phi_{3 \times 3}(U_{ps}(F_S + F_D))$. For tasks that do not require upsampling (e.g., denoising, deblurring and dehazing), we employ single convolution layer with residual connection to construct high-quality result, which can be formulated as $y' = \Phi_{3 \times 3}(F_S + F_D) + x$.

Loss Function: For image super-resolution, we use L_1 loss to optimize the network following [19, 28, 69], which can be formulated as

$$\mathcal{L} = \|y - y'\|_1,$$

where y is the target image. For image denoising, deblurring and dehazing, we adopt Charbonnier loss, i.e.,

$$\mathcal{L} = \sqrt{\|y - y'\|^2 + \epsilon^2},$$

where ϵ is a hyper-parameter and set to 10^{-3} empirically.

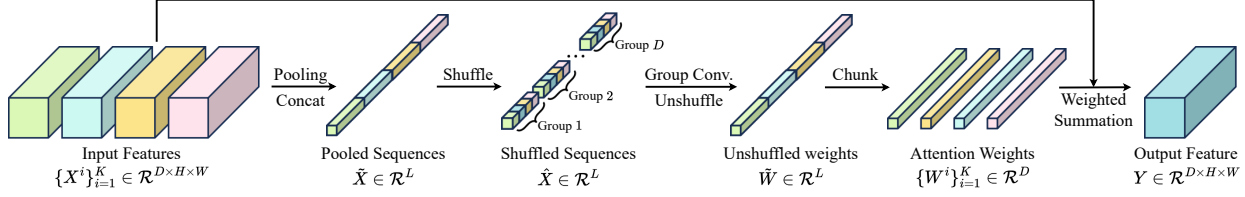


Figure 4. Illustration of the Sequence Shuffle Attention (SSA). The input features $\{X^i\}_{i=1}^K \in \mathcal{R}^{D \times H \times W}$ are first pooled and concatenated to form $\tilde{X} \in \mathcal{R}^L$, where $L = K \times D$. This sequence undergoes the sequence shuffle operation and results in shuffled sequences $\hat{X} \in \mathcal{R}^L$, whose channels are split by D group. Then, group convolution and sequence unshuffle operation are applied, producing unshuffled weights $\tilde{W} \in \mathcal{R}^L$, which are further chunked and reshaped into attention weights $\{W^i\}_{i=1}^K \in \mathcal{R}^D$. Finally, the output feature $Y \in \mathcal{R}^{D \times H \times W}$ is computed by performing a weighted summation of the input features using the attention weights.

3.2. MaIR Module

As elaborated above, MaIRM serves as the core module of MaIR, which involves a three-step pipeline. To be specific, MaIRM first flattens 2D features into four 1D sequences through NSS along four distinct directions following [32]. Then, MaIRM employs SSO to capture long-range dependencies. Finally, MaIRM aggregates processed sequences through SSA to form outputs. Mathematically, for input feature $F_{i,j}$, output feature $F_{i,j}^M$ can be formulated as

$$\begin{aligned} F_{i,j}^M &= M_{i,j}(F_{i,j}), \\ &= \Phi_{i,j}^{SSA}(\Phi_{i,j}^{SSO}(\Phi_{i,j}^{NSS}(F_{i,j}))), \end{aligned}$$

where $M_{i,j}(\cdot)$, $\Phi_{i,j}^{NSS}(\cdot)$, $\Phi_{i,j}^{SSO}(\cdot)$ and $\Phi_{i,j}^{SSA}(\cdot)$ are MaIRM, NSS, SSO and SSA in the j -th RMB of the i -th RMG, respectively.

NSS: NSS is designed to extract locality- and continuity-preserving sequences from input features. Motivated by the observation illustrated in Fig. 1, one could find that i) LocalMamba [22] preserves locality through restricted scanning region, and ii) Zigma [20] preserves continuity through S-shaped scanning path. Thus, as shown in Fig. 3(a), we design the nested S-shaped scanning strategy, which divides features into multiple non-overlapping stripes and uses S-shaped scanning path within and across stripes to maintain both locality and continuity. To better leverage spatial information, we extract sequences with four different scanning directions: top-left to bottom-right, bottom-right to top-left, top-right to bottom-left, and bottom-left to top-right, following previous works [19, 32].

Besides, NSS includes shift-stripe mechanism to preserve locality and continuity on the boundary regions between adjacent stripes. As depicted in Fig. 3(b), for two successive modules, the first module partitions features into multiple non-overlapping stripes with stripe width w_s . For the second module, we employ the shift-stripe operation, and set the first and last stripe widths as $\frac{w_s}{2}$ and others' width as w_s . Consequently, the boundary regions in the previous module will be fully covered by a single stripe in this module.

SSA: SSA aggregates the processed sequences by calculating attentions within corresponding channels. This de-

sign enables it to capture complex dependencies across distinct sequences, thus better leveraging complementary information from different scanning directions.

As shown in Fig. 4, supposing sequence number $K = 4$, for SSO-processed sequences $\{X^i\}_{i=1}^4$, we first apply spatial average pooling $\Phi_{AP}(\cdot)$ to reduce the computational cost, and then concatenate as

$$\begin{aligned} \tilde{X} &= \Phi_{cat}(\Phi_{AP}(\{X^i\}_{i=1}^4)) \\ &= [x_1^1, \dots, x_D^1, x_1^2, \dots, x_D^2, x_1^3, \dots, x_D^3, x_1^4, \dots, x_D^4], \end{aligned}$$

where x_d^k is the pooled feature in d -th channel of k -th sequence, and D is the number of channel in MaIRM. Then, we employ sequence shuffle operation $\Phi_{ss}(\cdot)$ to rearrange features into

$$\begin{aligned} \hat{X} &= \Phi_{ss}(X) \\ &= [x_1^1, x_1^2, x_1^3, x_1^4, x_2^1, x_2^2, x_2^3, x_2^4, \dots, x_D^1, x_D^2, x_D^3, x_D^4]. \end{aligned}$$

After that, we employ group convolution $\Phi_g(\cdot)$ with group size four to obtain the channel-wise attention weights and unshuffle the weights back to their original order, *i.e.*,

$$\begin{aligned} \tilde{W} &= \Phi_{su}(\Phi_g(\hat{X})) \\ &= [w_1^1, \dots, w_D^1, w_1^2, \dots, w_D^2, w_1^3, \dots, w_D^3, w_1^4, \dots, w_D^4], \end{aligned}$$

where $\Phi_{su}(\cdot)$ is sequence unshuffle operation. The unshuffled weights \tilde{W} are chunked as $\{W^i\}_{i=1}^4 = \Phi_{chunk}(\tilde{W})$, where $\Phi_{chunk}(\cdot)$ refers to the chunk operation. Finally, we adopt weight summation based on $\{W^i\}_{i=1}^4$ to generate the output, which can be formulated as:

$$Y = \sum_{i=1}^{K=4} W^i * X^i,$$

and Y is the output sequence of SSA.

4. Experiments

In this section, we evaluate our MaIR on four representative image restoration tasks, *i.e.*, image super-resolution, image denoising, image deblurring, and image dehazing. In the

Table 1. Quantitative results on classic image super-resolution. The best and second best results are in red and blue.

Methods	Scale	Set5		Set14		B100		Urban100		Manga109	
		PSNR	SSIM	PSNR	SSIM	PSNR	SSIM	PSNR	SSIM	PSNR	SSIM
SAN [11]	×2	38.31	0.9620	34.07	0.9213	32.42	0.9028	33.10	0.9370	39.32	0.9792
HAN [40]	×2	38.27	0.9614	34.16	0.9217	32.41	0.9027	33.35	0.9385	39.46	0.9785
IGNN [68]	×2	38.24	0.9613	34.07	0.9217	32.41	0.9025	33.23	0.9383	39.35	0.9786
NLSA [38]	×2	38.34	0.9618	34.08	0.9231	32.43	0.9027	33.42	0.9394	39.59	0.9789
ELAN [63]	×2	38.36	0.9620	34.20	0.9228	32.45	0.9030	33.44	0.9391	39.62	0.9793
IPT [4]	×2	38.37	-	34.43	-	32.48	-	33.76	-	-	-
SwinIR [28]	×2	38.42	0.9623	34.46	0.9250	32.53	0.9041	33.81	0.9427	39.92	0.9797
SRFormer [69]	×2	38.51	0.9627	34.44	0.9253	32.57	0.9046	34.09	0.9449	40.07	0.9802
MambaIR [19]	×2	38.57	0.9627	34.67	0.9261	32.58	0.9048	34.15	0.9446	40.28	0.9806
MaIR	×2	38.56	0.9628	34.75	0.9268	32.59	0.9049	34.19	0.9451	40.30	0.9807
MaIR+	×2	38.62	0.9630	34.82	0.9272	32.62	0.9053	34.38	0.9462	40.48	0.9811
SAN [11]	×3	34.75	0.9300	30.59	0.8476	29.33	0.8112	28.93	0.8671	34.30	0.9494
HAN [40]	×3	34.75	0.9299	30.67	0.8483	29.32	0.8110	29.10	0.8705	34.48	0.9500
IGNN [68]	×3	34.72	0.9298	30.66	0.8484	29.31	0.8105	29.03	0.8696	34.39	0.9496
NLSA [38]	×3	34.85	0.9306	30.70	0.8485	29.34	0.8117	29.25	0.8726	34.57	0.9508
ELAN [63]	×3	34.90	0.9313	30.80	0.8504	29.38	0.8124	29.32	0.8745	34.73	0.9517
IPT [4]	×3	34.81	-	30.85	-	29.38	-	29.49	-	-	-
SwinIR [28]	×3	34.97	0.9318	30.93	0.8534	29.46	0.8145	29.45	0.8826	35.12	0.9537
SRFormer [69]	×3	35.02	0.9323	30.94	0.8540	29.48	0.8156	30.04	0.8865	35.26	0.9543
MambaIR [19]	×3	35.08	0.9323	30.99	0.8536	29.51	0.8157	29.93	0.8841	35.43	0.9546
MaIR	×3	35.10	0.9324	31.05	0.8541	29.51	0.8160	30.05	0.8863	35.44	0.9547
MaIR+	×3	35.15	0.9328	31.12	0.8550	29.56	0.8167	30.24	0.8881	35.67	0.9556
SAN [11]	×4	32.64	0.9003	28.92	0.7888	27.78	0.7436	26.79	0.8068	31.18	0.9169
HAN [40]	×4	32.64	0.9002	28.90	0.7890	27.80	0.7442	26.85	0.8094	31.42	0.9177
IGNN [68]	×4	32.57	0.8998	28.85	0.7891	27.77	0.7434	26.84	0.8090	31.28	0.9182
NLSA [38]	×4	32.59	0.9000	28.87	0.7891	27.78	0.7444	26.96	0.8109	31.27	0.9184
ELAN [63]	×4	32.75	0.9022	28.96	0.7914	27.83	0.7459	27.13	0.8167	31.68	0.9226
IPT [4]	×4	32.64	-	29.01	-	27.82	-	27.26	-	-	-
SwinIR [28]	×4	32.92	0.9044	29.09	0.7950	27.92	0.7489	27.45	0.8254	32.03	0.9260
SRFormer [69]	×4	32.93	0.9041	29.08	0.7953	27.94	0.7502	27.68	0.8311	32.21	0.9271
MambaIR [19]	×4	33.03	0.9046	29.20	0.7961	27.98	0.7503	27.68	0.8287	32.32	0.9272
MaIR	×4	32.93	0.9045	29.20	0.7958	27.98	0.7507	27.71	0.8305	32.46	0.9284
MaIR+	×4	33.14	0.9058	29.28	0.7974	28.02	0.7516	27.89	0.8336	32.66	0.9297

following, we will first show quantitative results, and then conduct analysis studies to verify the reasonability. Experimental settings will be presented in the supplementary materials.

4.1. Results on Image Super-Resolution

In this section, we conduct experiments on both classic and lightweight image super-resolution.

Datasets: Following previous works [19, 28], we employ DF2K (DIV2K [49]+Flickr2K [30]) as the training set for classic image super-resolution, and DIV2K as training set for lightweight image super-resolution. For evaluation, we employ the following five datasets as test sets, *i.e.*, Set5 [3], Set14 [54], B100 [36], Urban100 [21] and

Manga109 [37]. Following existing works [11, 40, 58, 64], the low-resolution images are downsampled from the corresponding high-resolution images via bicubic interpolation.

Baselines: We compare our method with 15 competitive baselines. Specifically, we adopt four CNN-based methods (*i.e.*, SAN [11], HAN [40], IGNN [68], and NLSA [38]), four transformer-based methods (*i.e.*, ELAN [63], IPT [4], SwinIR [28] and SRFormer [69]) and one Mamba-based method (*i.e.*, MambaIR [19]) as the baselines for classic super-resolution. For lightweight super-resolution, four CNN-based methods (*i.e.*, CARN [2], IMDN [23], LAPPAR [27], LatticeNet [34]), two transformer-based methods (*i.e.*, SwinIR [28] and SRFormer [69]) and one Mamba-based method (*i.e.*, MambaIR [19]) are introduced into

Table 2. Quantitative results on lightweight image super-resolution. The best and second best results are in red and blue.

Methods	Scale	Params	MACs	Set5		Set14		B100		Urban100		Manga109	
				PSNR	SSIM	PSNR	SSIM	PSNR	SSIM	PSNR	SSIM	PSNR	SSIM
CARN [2]	×2	1,592K	222.8G	37.76	0.9590	33.52	0.9166	32.09	0.8978	31.92	0.9256	38.36	0.9765
IMDN [23]	×2	694K	158.8G	38.00	0.9605	33.63	0.9177	32.19	0.8996	32.17	0.9283	38.88	0.9774
LAPAR-A [27]	×2	548K	171.0G	38.01	0.9605	33.62	0.9183	32.19	0.8999	32.10	0.9283	38.67	0.9772
LatticeNet [34]	×2	756K	169.5G	38.15	0.9610	33.78	0.9193	32.25	0.9005	32.43	0.9302	-	-
SwinIR [28]	×2	910K	122.2G	38.14	0.9611	33.86	0.9206	32.31	0.9012	32.76	0.9340	39.12	0.9783
MambaIR-Tiny [19]	×2	905K	167.1G	38.13	0.9610	33.95	0.9208	32.31	0.9013	32.85	0.9349	39.20	0.9782
MaIR-Tiny	×2	878K	207.8G	38.18	0.9610	33.89	0.9209	32.31	0.9013	32.89	0.9346	39.22	0.9778
MambaIR-Small [19]	×2	1,363K	567.5G	38.16	0.9610	34.00	0.9212	32.34	0.9017	32.92	0.9356	39.31	0.9779
MaIR-Small	×2	1,355K	542.0G	38.20	0.9611	33.91	0.9209	32.34	0.9016	32.97	0.9359	39.32	0.9779
<hr/>													
CARN [2]	×3	1,592K	111.8G	34.29	0.9255	30.29	0.8407	29.06	0.8034	28.06	0.8493	33.50	0.9440
IMDN [23]	×3	703K	71.5G	34.36	0.9270	30.32	0.8417	29.09	0.8046	28.17	0.8519	33.61	0.9445
LAPAR-A [27]	×3	544K	144.0G	34.36	0.9267	30.34	0.8421	29.11	0.8054	28.15	0.8523	33.51	0.9441
LatticeNet [34]	×3	765K	76.3G	34.53	0.9281	30.39	0.8424	29.15	0.8059	28.33	0.8538	-	-
SwinIR [28]	×3	918K	55.4G	34.62	0.9289	30.54	0.8463	29.20	0.8082	28.66	0.8624	33.98	0.9478
MambaIR-Tiny [19]	×3	913K	74.5G	34.63	0.9288	30.54	0.8459	29.23	0.8084	28.70	0.8631	34.12	0.9479
MaIR-Tiny	×3	886K	93.0G	34.68	0.9292	30.54	0.8461	29.25	0.8088	28.83	0.8651	34.21	0.9484
MambaIR-Small [19]	×3	1,371K	252.7G	34.72	0.9296	30.63	0.8475	29.29	0.8099	29.00	0.8689	34.39	0.9495
MaIR-Small	×3	1,363K	241.4G	34.75	0.9300	30.63	0.8479	29.29	0.8103	28.92	0.8676	34.46	0.9497
<hr/>													
CARN [2]	×4	1,592K	90.9G	32.13	0.8937	28.60	0.7806	27.58	0.7349	26.07	0.7837	30.47	0.9084
IMDN [23]	×4	715K	40.9G	32.21	0.8948	28.58	0.7811	27.56	0.7353	26.04	0.7838	30.45	0.9075
LAPAR-A [27]	×4	659K	94.0G	32.15	0.8944	28.61	0.7818	27.61	0.7366	26.14	0.7871	30.42	0.9074
LatticeNet [34]	×4	777K	43.6G	32.30	0.8962	28.68	0.7830	27.62	0.7367	26.25	0.7873	-	-
SwinIR [28]	×4	930K	31.8G	32.44	0.8976	28.77	0.7858	27.69	0.7406	26.48	0.7980	30.92	0.9151
MambaIR-Tiny [19]	×4	924K	42.3G	32.42	0.8977	28.74	0.7847	27.68	0.7400	26.52	0.7983	30.94	0.9135
MaIR-Tiny	×4	897K	53.1G	32.48	0.8985	28.81	0.7864	27.71	0.7414	26.60	0.8013	31.13	0.9161
MambaIR-Small [19]	×4	1,383K	143.0G	32.51	0.8993	28.85	0.7876	27.75	0.7423	26.75	0.8051	31.26	0.9175
MaIR-Small	×4	1,374K	136.6G	32.62	0.8998	28.90	0.7882	27.77	0.7431	26.73	0.8049	31.34	0.9183

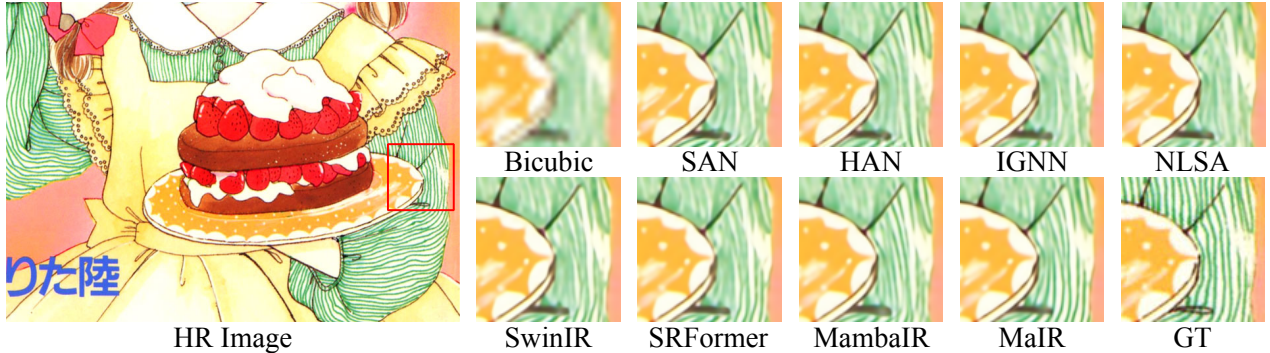


Figure 5. Visual comparison of $\times 4$ image super-resolution results on the Manga109 dataset. MaIR demonstrates superior visual quality, particularly in preserving fine details and textures.

both quantitative and qualitative comparisons. Similar to MambaIR, which offers two versions for lightweight super-resolution, MaIR is also available in two configurations: MaIR-Tiny and MaIR-Small.

Results: For classic super-resolution, as shown in Tab. 1 and Fig. 5, one could observe that MaIR achieves the best result in almost all quantitative comparisons. For instance, our method surpasses MambaIR [19] with 0.03dB~0.12dB in terms of PSNR on Urban100, and SRFormer with at most 0.04dB, 0.10dB and 0.25dB in terms of PSNR on B100, Urban100, and Manga109, respectively, which demonstrates the superiority of MaIR. For light-weight SR, MaIR also exhibits its advancement compared to baselines as reported in Tab. 2. Taking $\times 4$ scale as examples, MaIR-Small sur-

passes MambaIR-Small by 0.08dB in terms of PSNR on Manga109 with fewer parameters and MACs. MaIR-Tiny outperforms MambaIR-Tiny and SwinIR by 0.08dB and 0.12dB in terms of PSNR on Urban100 with fewer parameters, which verifies both the efficiency and effectiveness of our proposed method.

4.2. Results on Image Denoising

In this section, we evaluate MaIR on both synthetic Gaussian noise and real-world noise.

Datasets: For synthetic noise removal, we train MaIR on DFNB, which consists of DIV2K, Flickr2K, Waterloo Exploration Dataset (WED) [35] and BSD400 [36]. For evaluation, we utilize BSD68 [36], Kodak24, McMas-

Table 3. Quantitative results on gaussian color image denoising. The best and second best results are in red and blue.

Methods	BSD68			Kodak24			McMaster			Urban100		
	$\sigma=15$	$\sigma=25$	$\sigma=50$	$\sigma=15$	$\sigma=25$	$\sigma=50$	$\sigma=15$	$\sigma=25$	$\sigma=50$	$\sigma=15$	$\sigma=25$	$\sigma=50$
IRCNN [58]	33.86	31.16	27.86	34.69	32.18	28.93	34.58	32.18	28.91	33.78	31.20	27.70
FFDNet [59]	33.87	31.21	27.96	34.63	32.13	28.98	34.66	32.35	29.18	33.83	31.40	28.05
DnCNN [57]	33.90	31.24	27.95	34.60	32.14	28.95	33.45	31.52	28.62	32.98	30.81	27.59
DRUNet [61]	34.30	31.69	28.51	35.31	32.89	29.86	35.40	33.14	30.08	34.81	32.60	29.61
SwinIR [28]	34.42	31.78	28.56	35.34	32.89	29.79	35.61	33.20	30.22	35.13	32.90	29.82
Restormer [53]	34.40	31.79	28.60	35.47	33.04	30.01	35.61	33.34	30.30	35.13	32.96	30.02
CODE [66]	34.33	31.69	28.47	35.32	32.88	29.82	35.38	33.11	30.03	-	-	-
ART [56]	34.46	31.84	28.63	35.39	32.95	29.87	35.68	33.41	30.31	35.29	33.14	30.19
MambaIR [19]	34.43	31.80	28.61	35.34	32.91	29.85	35.62	33.35	30.31	35.17	32.99	30.07
MaIR	34.48	31.86	28.66	35.53	33.09	30.04	35.71	33.44	30.35	35.35	33.22	30.30
MaIR+	34.50	31.88	28.69	35.56	33.13	30.08	35.74	33.48	30.39	35.42	33.30	30.41

Table 4. Quantitative results on real image denoising. The best and second best results are in red and blue.

	DeamNet [43]	MPRNet [52]	NBNet [8]	DAGL [10]	Uformer [50]	MambaIR [19]	MaIR
PSNR	39.47	39.71	39.75	38.94	39.89	39.89	39.92
SSIM	0.957	0.958	0.959	0.953	0.960	0.960	0.960

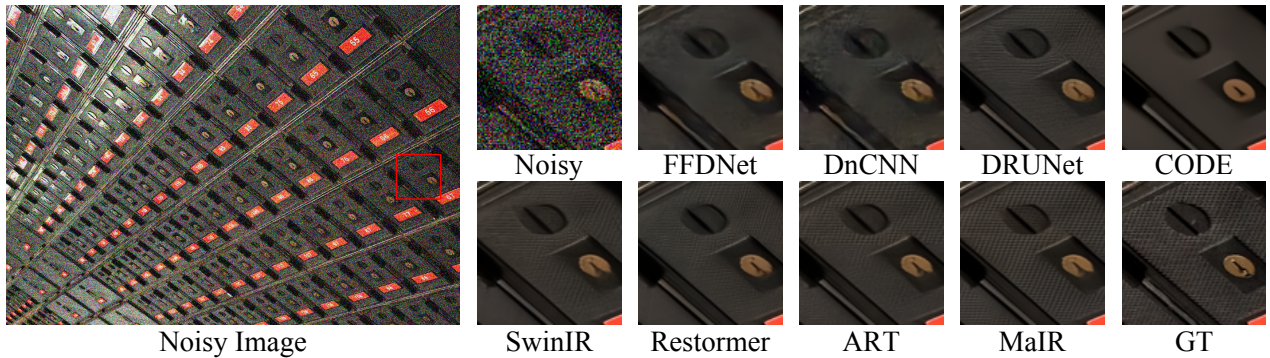


Figure 6. Visual comparison of image denoising results on the Urban100 dataset. MaIR effectively removes noise in the images and produces detailed textures that closely match the ground truth.

ter [62], and Urban100 as test set. Following [28, 57–59], we generate noisy images by manually adding white Gaussian noise to the clean images with three distinct noise levels, *i.e.*, $\sigma = 15, 25, 50$. For real-world image denoising, our model is trained and tested on the SIDD-Medium [1] dataset, which provides 320 high-resolution noisy-clean image pairs for training and additional 40 image pairs for test.

Baselines: We compare our MaIR with 14 representative methods. To be specific, we adopt four CNN-based methods (*i.e.*, IRCNN [58], FFDNet [59], DnCNN [57] and DRUNet [61]), four transformer-based methods (*i.e.*, SwinIR [28], Restormer [53], CODE [66] and ART [56]) and one Mamba-based method (*i.e.*, MambaIR [19]) as the baselines for synthetic noise removal. For real-world image denoising, four CNN-based methods (*i.e.*, Deam-

Net [43], MPRNet [52], NBNet [8] and DAGL [10]), two transformer-based methods (*i.e.*, Uformer [50] and Restormer [53]) and one Mamba-based method (*i.e.*, MambaIR [19]) are introduced for comparisons.

Results: As depicted in the Tab. 3-4, MaIR demonstrates superior performance on both synthetic and real-world image denoising compared to baselines. Taking results on Urban100 as examples, MaIR averagely outperforms MambaIR by 0.21dB in terms of PSNR, indicates its superiority on image denoising. Similar results can be derived from the qualitative comparisons shown in Fig. 6, MaIR could keep more detailed textures on the restored images, which are more closely to the ground truth.

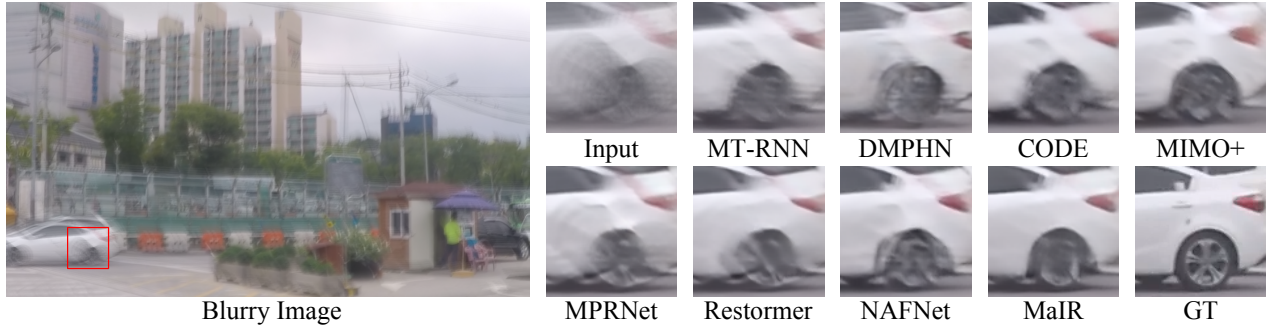


Figure 7. Visual comparison of motion deblurring results on the GoPro dataset. MaIR demonstrates superior performance in effectively removing motion blur while preserving precise fine details and textures, closely matching the ground truth.

Table 5. Quantitative results on image motion deblurring. The best and second best results are in red and blue. MACs in this table are evaluated on 128×128 patches followed [66].

Method	Params	MACs	GoPro	HIDE
SRN [48]	3.76M	35.87G	30.26	28.36
DBGAN [60]	11.59M	379.92G	31.10	28.94
MT-RNN [41]	2.64M	13.72G	31.15	29.15
DMPHN [55]	86.80M	-	31.20	29.09
CODE [66]	12.18M	22.52G	31.94	29.67
MIMO+ [9]	16.10M	38.64G	32.45	29.99
MPRNet [52]	20.13M	194.42G	32.66	30.96
Restormer [53]	26.13M	35.31G	32.92	31.22
Uformer [50]	50.88M	22.36G	33.06	30.90
CU-Mamba [13]	19.7M	-	33.53	31.47
NAFNet [6]	67.89M	15.85G	33.69	31.32
MaIR	26.29M	49.29G	33.69	31.57

4.3. Results on Image Deblurring

In this section, we evaluate MaIR on motion deblurring to verify the effectiveness of our proposed method.

Datasets: Following previous works [52, 53], we employ GoPro dataset [39] for training which consists of 2,103 blurry-clean image pairs. For evaluation, we use two common datasets, *i.e.*, GoPro test set and HIDE [45], which consist of 1,111 and 2,025 blurry-clean pairs, respectively.

Baselines: We adopt 11 competitive image deblurring baselines for comparisons. In detail, we adopt six CNN-based deblurring methods (*i.e.*, SRN [48], DBGAN [60], DMPHN [55], MIMO [9], MPRNet [52], and NAFNet [6]), three transformer-based methods (*i.e.*, CODE [66], Restormer [53] and Uformer [50]), one RNN-based method (*i.e.*, MT-RNN [41]) and one Mamba-based method (*i.e.*, CU-Mamba [13]) as the baselines.

Results: As shown in Tab. 5, proposed MaIR surpasses other baselines by PSNR on both GoPro and HIDE. In detail, MaIR outperforms Restormer [53] by 0.77dB on the GoPro dataset and by 0.35dB on the HIDE dataset in terms

of PSNR. Although NAFNet achieves similar quantitative results on GoPro, MaIR surpasses NAFNet on HIDE dataset by 0.25dB in terms of PSNR. As illustrated in Fig. 7, MaIR demonstrates its ability on handling heavily degraded areas, *i.e.*, MaIR could effectively remove blur and restore details around the wheels.

4.4. Results on Image Dehazing

In this section, we evaluate MaIR on image dehazing to verify the effectiveness of MaIR.

Datasets: Following existing works [47], we employ RESIDE dataset [25] for training and testing. For indoor scenes, we train MaIR on Indoor Training Set (ITS) which consists of 13,990 hazy-clean pairs, and test it on indoor synthetic objective testing set (SOTS-Indoor) involving 500 pairs. For outdoor scenes, we train MaIR on Outdoor Training Set (OTS), which contains 313,950 image pairs, and evaluate it on outdoor synthetic objective testing set (SOTS-Outdoor) involving 500 images. In addition, to verify MaIR on more general cases, we also train the model on RESIDE-6K and test it on the SOTS-mix, which mix both indoor and outdoor images.

Baselines: We adopt eight competitive methods as baselines. Specifically, we adopt five CNN-based image dehazing methods (*i.e.*, AODNet [24], GDN [31], MSBDN [14], FFANet [42] and AECRNet [51]), two transformer-based methods (*i.e.*, Dehazer [18], Dehazeformer [47]) and one Mamba-based method (*i.e.*, UVM-Net [67]) as baselines.

Results: As shown in Tab. 6 and Fig. 8, our MaIR surpasses most baselines on both quantitative and qualitative comparisons. Taking quantitative results as examples, MaIR significantly outperforms DehazeFormer and UVM-Net by 2.67dB and 2.04dB in terms of PSNR on the outdoor scenes. Although UVM-Net is slightly higher on PSNR in the indoor scenes, MaIR only takes 0.3% and 4.8% params and MACs of the UVM-Net, which verifies both effectiveness and efficiency.

Table 6. Quantitative results on image dehazing. The best and second best results are in red and blue. MACs in this table are evaluated on 256×256 patches followed [47, 67].

Method	AODNet [24]	GDN [31]	MSBDN [14]	FFANet [42]	AECRNet [51]	Dehamer [18]	DehazeFormer [47]	UVM-Net [67]	MaIR (Ours)
Params	0.002M	0.96M	31.35M	4.46M	2.61M	132.45M	4.63M	1,003.94M	3.40M
MACs	0.115G	21.49G	41.54G	287.8G	52.20G	48.93G	48.64G	501.91G	24.03G
SOTS-Indoor	PSNR: 20.51 SSIM: 0.816	PSNR: 32.16 SSIM: 0.984	PSNR: 33.67 SSIM: 0.985	PSNR: 36.39 SSIM: 0.989	PSNR: 37.17 SSIM: 0.990	PSNR: 36.63 SSIM: 0.988	PSNR: 38.46 SSIM: 0.994	PSNR: 40.17 SSIM: 0.996	PSNR: 39.45 SSIM: 0.997
SOTS-Outdoor	PSNR: 24.14 SSIM: 0.920	PSNR: 30.86 SSIM: 0.982	PSNR: 33.48 SSIM: 0.982	PSNR: 33.57 SSIM: 0.984	-	PSNR: 35.18 SSIM: 0.986	PSNR: 34.29 SSIM: 0.983	PSNR: 34.92 SSIM: 0.984	PSNR: 36.96 SSIM: 0.991
SOTS-Mix	PSNR: 20.27 SSIM: 0.855	PSNR: 25.86 SSIM: 0.944	PSNR: 28.56 SSIM: 0.966	PSNR: 29.96 SSIM: 0.973	PSNR: 28.52 SSIM: 0.964	-	PSNR: 30.89 SSIM: 0.977	PSNR: 31.92 SSIM: 0.982	PSNR: 31.52 SSIM: 0.980

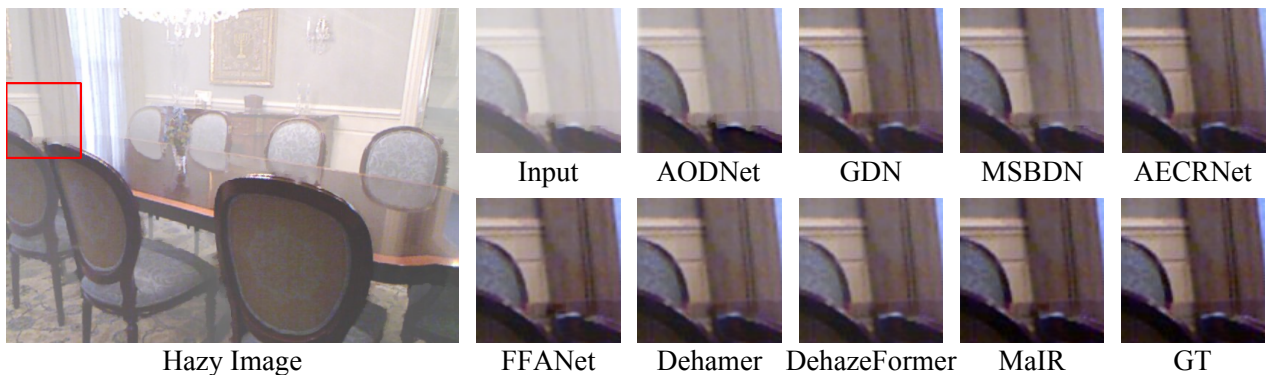


Figure 8. Visual comparison of image dehazing results on the SOTS dataset. MaIR can effectively remove haze and restore content with colors that closely match the ground truth.

Table 7. Ablation study on the proposed NSS scheme, tested on lightweight super-resolution tasks with scale factor $\times 2$. The results on the Urban100 dataset are presented, which demonstrates the effectiveness of the NSS.

	Baseline	w/o NSS	w/o SS	LM	ZigMa	Hilbert
PSNR	32.97	32.94	32.93	32.93	32.88	32.95
SSIM	0.9359	0.9355	0.9351	0.9357	0.9354	0.9356

4.5. Analysis Experiments

In this section, we first conduct ablation studies to verify the effectiveness of the NSS and SSA. Then, we introduce analysis experiments to investigate the impact of stripe width on the overall performance.

4.5.1. Ablation Studies

We first conduct ablation study to analyze the effectiveness of NSS. In detail, five configurations are conducted, i) replacing NSS with Z-shaped scanning strategy (denoted as w/o NSS), ii) removing shift stripe (denoted as w/o SS), iii) replacing NSS with the scanning strategy in LocalMamba [22] (denoted as LM), iv) replacing NSS by the scanning strategy in ZigMa [20] (denoted as ZigMa) and v) replacing NSS by the Hilbert curve (denoted as Hilbert).

Table 8. Ablation study on SSA for lightweight super-resolution with scale factor $\times 2$. The results on Urban100 dataset are presented, which demonstrates the effectiveness of the NSS.

	Baseline	w.o. SSA	Gating
PSNR	32.97	32.90	32.92
SSIM	0.9359	0.9350	0.9252

Table 9. Analyses on stripe widths. Experiment was conducted on the Urban100 dataset with a scale factor $\times 2$ for lightweight super-resolution tasks, which illustrates how changes in stripe width affect the restored image quality.

	2	4	8	16	32
PSNR	32.95	32.97	32.97	32.97	32.92
SSIM	0.9356	0.9359	0.9355	0.9357	0.9355

As illustrated in Tab. 7, one could see that NSS is important to improve the performance of MaIR.

To investigate the effectiveness of SSA, we also conduct experiments under the following settings: i) removing proposed SSA and aggregating sequences via sequences-wise addition (termed as w.o. SSA), and ii) replacing SSA by the gating strategy in [5] (termed as Gating). As reported in Tab. 8, SSA is more effective than others.

4.5.2. Results on different stripe width

To investigate influence of stripe width, we train lightweight SR model with various stripe width (2, 4, 8, 16 and 32) and evaluate them on Urban100 dataset. As presented in Tab. 9, one could observe that the PSNR and SSIM values are quite similar under different settings, except for the cases with the largest and the smallest stripe widths. It indicates that the proposed method exhibits robustness against changes in stripe width, maintaining high-quality image restoration across a range of stripe widths.

5. Conclusion

In this paper, we propose MaIR, a novel state space model for image restoration that can preserve both local dependencies and spatial continuity of input images. To this end, we propose two designs: Nested S-shaped Scanning strategy (NSS) and Sequences Shuffle Attention (SSA). NSS is designed to extract locality- and continuity-preserving sequences from images, and SSA adaptively aggregates these sequences. Thanks to their cooperation, MaIR not only addresses the limitations of existing Mamba-based restoration methods but also improves image quality without introducing extra computations. Extensive experiments across four tasks on 14 benchmarks comparing with 40 baselines, validate the superiority of MaIR, demonstrating its robustness and effectiveness in various image restoration tasks.

References

- [1] Abdelrahman Abdelhamed, Stephen Lin, and Michael S Brown. A high-quality denoising dataset for smartphone cameras. In *Proceedings of the IEEE conference on computer vision and pattern recognition*, pages 1692–1700, 2018. 7
- [2] Namhyuk Ahn, Byungkon Kang, and Kyung-Ah Sohn. Fast, accurate, and lightweight super-resolution with cascading residual network. In *Proceedings of the European conference on computer vision (ECCV)*, pages 252–268, 2018. 5, 6
- [3] Marco Bevilacqua, Aline Roumy, Christine Guillemot, and Marie Line Alberi-Morel. Low-complexity single-image super-resolution based on nonnegative neighbor embedding, 2012. 5
- [4] Hanting Chen, Yunhe Wang, Tianyu Guo, Chang Xu, Yiping Deng, Zhenhua Liu, Siwei Ma, Chunjing Xu, Chao Xu, and Wen Gao. Pre-Trained Image Processing Transformer. In *IEEE Conference on Computer Vision and Pattern Recognition*, pages 12299–12310, Virtual, 2021. 5
- [5] Keyan Chen, Bowen Chen, Chenyang Liu, Wenyuan Li, Zhengxia Zou, and Zhenwei Shi. Rsmamba: Remote sensing image classification with state space model. *IEEE Geoscience and Remote Sensing Letters*, 2024. 9
- [6] Liangyu Chen, Xiaojie Chu, Xiangyu Zhang, and Jian Sun. Simple baselines for image restoration. In *European conference on computer vision*, pages 17–33. Springer, 2022. 8
- [7] Xiangyu Chen, Xintao Wang, Jiantao Zhou, Yu Qiao, and Chao Dong. Activating more pixels in image super-resolution transformer. In *Proceedings of the IEEE/CVF conference on computer vision and pattern recognition*, pages 22367–22377, 2023. 2
- [8] Shen Cheng, Yuzhi Wang, Haibin Huang, Donghao Liu, Haoqiang Fan, and Shuaicheng Liu. Nbnnet: Noise basis learning for image denoising with subspace projection. In *Proceedings of the IEEE/CVF conference on computer vision and pattern recognition*, pages 4896–4906, 2021. 7
- [9] Sung-Jin Cho, Seo-Won Ji, Jun-Pyo Hong, Seung-Won Jung, and Sung-Jea Ko. Rethinking coarse-to-fine approach in single image deblurring. In *Proceedings of the IEEE/CVF international conference on computer vision*, pages 4641–4650, 2021. 2, 8
- [10] Mou Chong, Zhang Jian, and Wu Zhuoyuan. Dynamic attentive graph learning for image restoration. In *IEEE International Conference on Computer Vision*, 2021. 7
- [11] Tao Dai, Jianrui Cai, Yongbing Zhang, Shu-Tao Xia, and Lei Zhang. Second-order attention network for single image super-resolution. In *IEEE Conference on Computer Vision and Pattern Recognition*, pages 11065–11074, 2019. 2, 5
- [12] Tri Dao and Albert Gu. Transformers are SSMs: Generalized models and efficient algorithms through structured state space duality. In *International Conference on Machine Learning (ICML)*, 2024. 2
- [13] Rui Deng and Tianpei Gu. Cu-mamba: Selective state space models with channel learning for image restoration. *arXiv preprint arXiv:2404.11778*, 2024. 2, 8
- [14] Hang Dong, Jinshan Pan, Lei Xiang, Zhe Hu, Xinyi Zhang, Fei Wang, and Ming-Hsuan Yang. Multi-Scale Boosted Dehazing Network with Dense Feature Fusion. In *IEEE Conference on Computer Vision and Pattern Recognition*, pages 2154–2164, Seattle, WA, 2020. 8, 9
- [15] Yuanbiao Gou, Boyun Li, Zitao Liu, Songfan Yang, and Xi Peng. Clearer: Multi-scale neural architecture search for image restoration. *Advances in Neural Information Processing Systems*, 33, 2020. 2
- [16] Albert Gu and Tri Dao. Mamba: Linear-time sequence modeling with selective state spaces. *arXiv preprint arXiv:2312.00752*, 2023. 2
- [17] Albert Gu, Karan Goel, and Christopher Ré. Efficiently modeling long sequences with structured state spaces. *arXiv preprint arXiv:2111.00396*, 2021. 2
- [18] Chun-Le Guo, Qixin Yan, Saeed Anwar, Runmin Cong, Wenqi Ren, and Li Chongyi. Image dehazing transformer with transmission-aware 3d position embedding. In *Proceedings of the IEEE/CVF Conference on Computer Vision and Pattern Recognition*, 2022. 8, 9
- [19] Hang Guo, Jinmin Li, Tao Dai, Zhihao Ouyang, Xudong Ren, and Shu-Tao Xia. Mambair: A simple baseline for image restoration with state-space model. *arXiv preprint arXiv:2402.15648*, 2024. 2, 3, 4, 5, 6, 7
- [20] Vincent Tao Hu, Stefan Andreas Baumann, Ming Gui, Olga Grebenkova, Pingchuan Ma, Johannes S Fischer, and Björn Ommer. Zigma: A dit-style zigzag mamba diffusion model. *arXiv preprint arXiv:2403.13802*, 2024. 3, 4, 9

- [21] Jia-Bin Huang, Abhishek Singh, and Narendra Ahuja. Single image super-resolution from transformed self-exemplars. In *Proceedings of the IEEE conference on computer vision and pattern recognition*, pages 5197–5206, 2015. 5
- [22] Tao Huang, Xiaohuan Pei, Shan You, Fei Wang, Chen Qian, and Chang Xu. Localmamba: Visual state space model with windowed selective scan. *arXiv preprint arXiv:2403.09338*, 2024. 2, 3, 4, 9
- [23] Zheng Hui, Xinbo Gao, Yunchu Yang, and Xiumei Wang. Lightweight image super-resolution with information multi-distillation network. In *Proceedings of the 27th acm international conference on multimedia*, pages 2024–2032, 2019. 5, 6
- [24] Boyi Li, Xiulian Peng, Zhangyang Wang, Jizheng Xu, and Dan Feng. AOD-Net: All-in-One Dehazing Network. In *IEEE International Conference on Computer Vision*, pages 4780–4788, Venice, Italy, 2017. 8, 9
- [25] Boyi Li, Wenqi Ren, Dengpan Fu, Dacheng Tao, Dan Feng, Wenjun Zeng, and Zhangyang Wang. Benchmarking Single Image Dehazing and Beyond. *IEEE Transactions on Image Processing*, 28(1):492–505, 2019. 8
- [26] Boyun Li, Xiao Liu, Peng Hu, Zhongqin Wu, Jiancheng Lv, and Xi Peng. All-In-One Image Restoration for Unknown Corruption. In *IEEE Conference on Computer Vision and Pattern Recognition*, pages 17431–17441, New Orleans, LA, 2022. 2
- [27] Wenbo Li, Kun Zhou, Lu Qi, Nianjuan Jiang, Jiangbo Lu, and Jiaya Jia. Lapar: Linearly-assembled pixel-adaptive regression network for single image super-resolution and beyond. *Advances in Neural Information Processing Systems*, 33:20343–20355, 2020. 2, 5, 6
- [28] Jingyun Liang, Jiezhong Cao, Guolei Sun, Kai Zhang, Luc Van Gool, and Radu Timofte. SwinIR: Image Restoration Using Swin Transformer. In *International Conference on Computer Vision Workshops*, Virtual, 2021. 2, 3, 5, 6, 7
- [29] Bee Lim, Sanghyun Son, Heewon Kim, Seungjun Nah, and Kyoung Mu Lee. Enhanced deep residual networks for single image super-resolution. In *IEEE Conference on Computer Vision and Pattern Recognition Workshop*, pages 1132–1140, 2017. 2
- [30] Bee Lim, Sanghyun Son, Heewon Kim, Seungjun Nah, and Kyoung Mu Lee. Enhanced deep residual networks for single image super-resolution. In *Proceedings of the IEEE conference on computer vision and pattern recognition workshops*, pages 136–144, 2017. 5
- [31] Xiaohong Liu, Yongrui Ma, Zhihao Shi, and Jun Chen. Grid-DehazeNet: Attention-Based Multi-Scale Network for Image Dehazing. In *International Conference on Computer Vision*, pages 7313–7322, Seoul, Korea, 2019. 8, 9
- [32] Yue Liu, Yunjie Tian, Yuzhong Zhao, Hongtian Yu, Lingxi Xie, Yaowei Wang, Qixiang Ye, and Yunfan Liu. Vmamba: Visual state space model. *arXiv preprint arXiv:2401.10166*, 2024. 2, 4
- [33] Ze Liu, Yutong Lin, Yue Cao, Han Hu, Yixuan Wei, Zheng Zhang, Stephen Lin, and Baining Guo. Swin transformer: Hierarchical vision transformer using shifted windows. In *Proceedings of the IEEE/CVF international conference on computer vision*, pages 10012–10022, 2021. 2
- [34] Xiaotong Luo, Yuan Xie, Yulun Zhang, Yanyun Qu, Cuihua Li, and Yun Fu. Latticenet: Towards lightweight image super-resolution with lattice block. In *European Conference on Computer Vision*, pages 272–289, 2020. 5, 6
- [35] Kede Ma, Zhengfang Duanmu, Qingbo Wu, Zhou Wang, Hongwei Yong, Hongliang Li, and Lei Zhang. Waterloo Exploration Database: New Challenges for Image Quality Assessment Models. *IEEE Transactions on Image Processing*, 26(2):1004–1016, 2017. 6
- [36] David Martin, Charless Fowlkes, Doron Tal, and Jitendra Malik. A Database of Human Segmented Natural Images and its Application to Evaluating Segmentation Algorithms and Measuring Ecological Statistics. In *International Conference on Computer Vision*, pages 416–425, Vancouver, Canada, 2001. 5, 6
- [37] Yusuke Matsui, Kota Ito, Yuji Aramaki, Azuma Fujimoto, Toru Ogawa, Toshihiko Yamasaki, and Kiyoharu Aizawa. Sketch-based manga retrieval using manga109 dataset. *Multimedia tools and applications*, 76:21811–21838, 2017. 5
- [38] Yiqun Mei, Yuchen Fan, and Yuqian Zhou. Image super-resolution with non-local sparse attention. In *IEEE Conference on Computer Vision and Pattern Recognition*, pages 3517–3526, 2021. 5
- [39] Seungjun Nah, Tae Hyun Kim, and Kyoung Mu Lee. Deep Multi-scale Convolutional Neural Network for Dynamic Scene Deblurring. In *IEEE Conference on Computer Vision and Pattern Recognition*, pages 257–265, Honolulu, HI, 2017. 2, 8
- [40] Ben Niu, Weiwei Wen, Wenqi Ren, Xiangde Zhang, Lianping Yang, Shuzhen Wang, Kaihao Zhang, Xiaochun Cao, and Haifeng Shen. Single image super-resolution via a holistic attention network. In *European Conference on Computer Vision*, pages 191–207, 2020. 2, 5
- [41] Dongwon Park, Dong Un Kang, Jisoo Kim, and Se Young Chun. Multi-temporal recurrent neural networks for progressive non-uniform single image deblurring with incremental temporal training. In *European Conference on Computer Vision*, pages 327–343. Springer, 2020. 8
- [42] Xu Qin, Zhilin Wang, Yuanchao Bai, Xiaodong Xie, and Huizhu Jia. FFA-Net: Feature Fusion Attention Network for Single Image Dehazing. In *AAAI Conference on Artificial Intelligence*, pages 11908–11915, New York, NY, 2020. 8, 9
- [43] Chao Ren, Xiaohai He, Chuncheng Wang, and Zhibo Zhao. Adaptive consistency prior based deep network for image denoising. In *Proceedings of the IEEE/CVF conference on computer vision and pattern recognition*, pages 8596–8606, 2021. 7
- [44] Christos Sakaridis, Dengxin Dai, and Luc Van Gool. Semantic foggy scene understanding with synthetic data. *International Journal of Computer Vision*, 126(9):973–992, 2018. 2
- [45] Ziyi Shen, Wenguan Wang, Xiankai Lu, Jianbing Shen, Haibin Ling, Tingfa Xu, and Ling Shao. Human-aware motion deblurring. In *Proceedings of the IEEE/CVF international conference on computer vision*, pages 5572–5581, 2019. 8
- [46] Jimmy TH Smith, Andrew Warrington, and Scott Linderman. Simplified state space layers for sequence modeling.

- In *The Eleventh International Conference on Learning Representations*, 2022. 2
- [47] Yuda Song, Zhuqing He, Hui Qian, and Xin Du. Vision transformers for single image dehazing. *IEEE Transactions on Image Processing*, 32:1927–1941, 2023. 8, 9
- [48] Xin Tao, Hongyun Gao, Xiaoyong Shen, Jue Wang, and Jiaya Jia. Scale-recurrent network for deep image deblurring. In *Proceedings of the IEEE conference on computer vision and pattern recognition*, pages 8174–8182, 2018. 2, 8
- [49] Radu Timofte, Eirikur Agustsson, Luc Van Gool, Ming-Hsuan Yang, and Lei Zhang. Ntire 2017 challenge on single image super-resolution: Methods and results. In *Proceedings of the IEEE conference on computer vision and pattern recognition workshops*, pages 114–125, 2017. 5
- [50] Zhendong Wang, Xiaodong Cun, Jianmin Bao, Wengang Zhou, Jianzhuang Liu, and Houqiang Li. Uformer: A general u-shaped transformer for image restoration. In *Proceedings of the IEEE/CVF Conference on Computer Vision and Pattern Recognition (CVPR)*, pages 17683–17693, 2022. 7, 8
- [51] Haiyan Wu, Yanyun Qu, Shaohui Lin, Jian Zhou, Ruizhi Qiao, Zhizhong Zhang, Yuan Xie, and Lizhuang Ma. Contrastive Learning for Compact Single Image Dehazing. In *IEEE Conference on Computer Vision and Pattern Recognition*, pages 10551–10560, Virtual, 2021. 8, 9
- [52] Syed Waqas Zamir, Aditya Arora, Salman Khan, Munawar Hayat, Fahad Shahbaz Khan, Ming-Hsuan Yang, and Ling Shao. Multi-Stage Progressive Image Restoration. In *IEEE Conference on Computer Vision and Pattern Recognition*, pages 14821–14831, Virtual, 2021. 7, 8
- [53] Syed Waqas Zamir, Aditya Arora, Salman Khan, Munawar Hayat, Fahad Shahbaz Khan, and Ming-Hsuan Yang. Restormer: Efficient Transformer for High-Resolution Image Restoration. In *IEEE Conference on Computer Vision and Pattern Recognition*, pages 5718–5729, New Orleans, LA, 2022. 2, 7, 8
- [54] Roman Zeyde, Michael Elad, and Matan Protter. On single image scale-up using sparse-representations. In *Curves and Surfaces: 7th International Conference, Avignon, France, June 24-30, 2010, Revised Selected Papers 7*, pages 711–730. Springer, 2012. 5
- [55] Hongguang Zhang, Yuchao Dai, Hongdong Li, and Piotr Koniusz. Deep stacked hierarchical multi-patch network for image deblurring. In *Proceedings of the IEEE/CVF conference on computer vision and pattern recognition*, pages 5978–5986, 2019. 8
- [56] Jiale Zhang, Yulun Zhang, Jinjin Gu, Yongbing Zhang, Linghe Kong, and Xin Yuan. Accurate image restoration with attention retractable transformer. In *ICLR*, 2023. 7
- [57] Kai Zhang, Wangmeng Zuo, Yunjin Chen, Deyu Meng, and Lei Zhang. Beyond a Gaussian Denoiser: Residual Learning of Deep CNN for Image Denoising. *IEEE Transactions on Image Processing*, 26(7):3142–3155, 2017. 2, 7
- [58] Kai Zhang, Wangmeng Zuo, Shuhang Gu, and Lei Zhang. Learning deep cnn denoiser prior for image restoration. In *IEEE Conference on Computer Vision and Pattern Recognition*, pages 3929–3938, 2017. 5, 7
- [59] Kai Zhang, Wangmeng Zuo, and Lei Zhang. Ffdnet: Toward a fast and flexible solution for CNN based image denoising. *IEEE Transactions on Image Processing*, 2018. 7
- [60] Kaihao Zhang, Wenhan Luo, Yiran Zhong, Lin Ma, Bjorn Stenger, Wei Liu, and Hongdong Li. Deblurring by realistic blurring. In *Proceedings of the IEEE/CVF conference on computer vision and pattern recognition*, pages 2737–2746, 2020. 2, 8
- [61] Kai Zhang, Yawei Li, Wangmeng Zuo, Lei Zhang, Luc Van Gool, and Radu Timofte. Plug-and-play image restoration with deep denoiser prior. *IEEE Transactions on Pattern Analysis and Machine Intelligence*, 44(10):6360–6376, 2021. 7
- [62] Lei Zhang, Xiaolin Wu, Antoni Buades, and Xin Li. Color demosaicking by local directional interpolation and nonlocal adaptive thresholding. *Journal of Electronic imaging*, 20(2):023016–023016, 2011. 7
- [63] Xindong Zhang, Hui Zeng, Shi Guo, and Lei Zhang. Efficient long-range attention network for image super-resolution. In *European Conference on Computer Vision*, pages 649–667. Springer, 2022. 5
- [64] Yulun Zhang, Kungpeng Li, Kai Li, Lichen Wang, Bineng Zhong, and Yun Fu. Image super-resolution using very deep residual channel attention networks. In *European Conference on Computer Vision*, pages 294–310, 2018. To appear in ECCV 2018. 2, 5
- [65] Yulun Zhang, Yapeng Tian, Yu Kong, Bineng Zhong, and Yun Fu. Residual Dense Network for Image Restoration. *IEEE Transactions on Pattern Analysis and Machine Intelligence*, 43(7):2480–2495, 2018. 2
- [66] Haiyu Zhao, Yuanbiao Gou, Boyun Li, Dezhong Peng, Jiancheng Lv, and Xi Peng. Comprehensive and delicate: An efficient transformer for image restoration. In *Proceedings of the IEEE/CVF Conference on Computer Vision and Pattern Recognition*, pages 14122–14132, 2023. 2, 7, 8
- [67] Zhuoran Zheng and Chen Wu. U-shaped vision mamba for single image dehazing. *arXiv preprint arXiv:2402.04139*, 2024. 2, 3, 8, 9
- [68] Shangchen Zhou, Jiawei Zhang, Wangmeng Zuo, and Chen Change Loy. Cross-scale internal graph neural network for image super-resolution. In *Neural Information Processing Systems*, 2020. NeurIPS 2020. 5
- [69] Yupeng Zhou, Zhen Li, Chun-Le Guo, Song Bai, Ming-Ming Cheng, and Qibin Hou. Srformer: Permuted self-attention for single image super-resolution. In *IEEE Conference on Computer Vision and Pattern Recognition*, pages 12780–12791, 2023. 3, 5
- [70] Lianghui Zhu, Bencheng Liao, Qian Zhang, Xinlong Wang, Wenyu Liu, and Xinggang Wang. Vision mamba: Efficient visual representation learning with bidirectional state space model. *arXiv preprint arXiv:2401.09417*, 2024. 2